ARTICLE

Journal of Micromechanics and Molecular Physics

Viscoelastic behavior in discrete element method realized by interparticle Maxwell–Zener model

A. Wahn[*,‡], **Y. Gan**[†] **& M. Kamlah**[*]

Abstract The discrete element method describes the motion of granular structures numerically. Each particle is considered as a discrete element. Combining springs and dashpot for the normal contact forces, viscoelastic behavior represented by rheological models is realized via a nonlinear Maxwell–Zener model in a dynamic routine. For individual contacts and large particle structures, this model is compared to the Hertzian contact model for elastic behavior and studied with respect to rate dependence and the effect of model parameters.

Keywords Discrete element method; granular materials; viscoelastic contact model.

1. Introduction

The discrete element method (DEM) is particularly suitable for calculating motion sequences and deformations of granular materials, i.e. materials containing discontinuous structures, first introduced by Cundall and Strack [1] in the 1970s. Unlike continuum mechanics approaches, such as the finite element method (FEM), the assumption of a discrete element applies to each granular particle without locally resolving fields inside, e.g. stress, strain and/or temperature. Each element is uniquely defined by its position, shape, orientation and size. This makes DEM a computationally efficient tool which enables the study of systems consisting of many particles.

In DEM, Newton's equations of motion are solved under the action of contact forces and moments. It uses suitable contact models to capture the interparticle forces as realistically as possible. The most commonly used contact law in DEM simulations is the Hertzian law [2], representing the behavior of a nonlinear spring and describes an elastic contact. An even simpler approach is offered by the model of a linear spring, which displays a linear elastic contact behavior [3,4]. Several existing contact models in DEM framework have been reviewed in Ref. 5, whilst interparticle model should consider normal, tangential, rolling and twist motions between two particles. Besides statistics on quantities on particle level like contact forces, coordination number, particle velocities, packing factor, etc., macroscopic stresses and deformation states can be computed through homogenization schemes [6].

As a result, DEM has been increasingly used for many applications in recent years. To name only a few, these include the simulation of mixing and segregation processes [7,8], the analysis of fluidized beds and silo discharge [9–11], pneumatic conveying and particulate flow in pipes [12], pebble assemblies for nuclear fuels [13] and milling [14]. The method is proven to have numerous advantages relating to accuracy and numerical stability but it also needs constant improvement. This includes the contact formulations regarding to the dissipation of energy. In many applications, inelastic contact behavior is already investigated [15–19]. Thornton *et al.* [15,16] developed an inelastic contact model for spherical shaped bodies in which an elasticity phase from a plasticity phase has been distinguished. A similar model by Martin [17] takes adhesion of particles into account. Further examples include: the effect of elastoplastic [18] and quasi-plastic behavior of active material particles in lithium-ion batteries (LIBs) [19].

The cathode of an LIB has a granular structure on microscopic level consisting of single active material particles whose interactions are influenced by the overall structure [20]. A mixture of conductive additives, typically carbon black which improves the electronic conductivity of the entire electrode, and a binder is located in the pore space of active particles [21]. The small particles can display elastic or elastoplastic material behavior, yet most existing DEM studies focused mainly elastic behavior for understanding the mechanical responses and effective conductivity under various operational conditions [22].

During the manufacturing step called calendaring [20], the electrode is mechanically compressed, in order to obtain electronic conduction paths between the active material particles and conductive additive particles [23]. The compacted state is strongly influenced by the material behavior of the different components as well as their mechanical interactions [24]. In particular, typical binder materials can introduce viscoelastic material behavior into the particle assembly of the electrode. This time-dependent behavior

[*]Karlsruhe Institute of Technology, Institute for Applied Materials, Eggenstein-Leopoldshafen 76344, Germany
[†]School od Civil Engineering, and The University of Sydney Nano Institute, The University of Sydney, NSW 2006, Australia
[‡]Alexandra.wahn@kit.edu
[‡]Corresponding author.

Received 29 March 2022; Revised 9 June 2022; Accepted 11 June 2022; Published 18 July 2022; doi:10.1142/S2424913022410053

has to be reflected in DEM simulations for calendaring [25]. Motivated by this, this work focuses on investigating viscoelastic contact behavior of individual granular particles on a micro level, and aims to implement this interparticle behavior in the DEM framework. The calculation of viscoelastic contact forces can be used, for example, in the simulation of the calendaring of an LIB cathode, where the viscoelastic binder and the elastic active material determine the material behavior.

Regarding the contact problem of viscoelastic bodies only, Lee and Radok have pioneered the development of analytical solutions [26]. Johnson [27] presents Radok's idea [28] of describing the contact behavior of linearly viscoelastic bodies with stress−strain relations under the condition that an associated perfectly elastic solution exists. According to Radok [28], the elasticity constants in the elasticity solution can be replaced by the corresponding integral operators of the viscoelastic stress−strain relation.

Olson (2002) used this approach in Ref. 29 to describe particle damping in more details, where the particle dynamics method is used and compared to experiments regarding to a cantilevered aluminum beam under the influence of variable impacts. For asphalt mixture Liu *et al.* [30] developed a viscoelastic DEM approach using a Burger's model over cyclic loadings. Also other investigators studied the contact behavior between viscoelastic spherical particles based on the theory of Hertz [2] for normal contact and the theory of Mindlin−Deresiewicz (MD) [31,32] for frictional contact [33−35]. Some related work ca be found in Refs. 36 and 37.

In this paper, we present a comparison of two approaches to model the compaction behavior under the action of viscoelastic contact forces where inertia effects can still be neglected as in the calendaring process. The first one is a quasi-static routine, which represents infinitely slow procedures and pursues a sequence of relaxed static equilibrium states. In this case, "time" has the only meaning of the sequence of the equilibrium states. The second approach is a dynamic routine, which is dependent on physical time, such that viscoelastic effects can be accounted for.

Concerning the methods of this work, we first recall some basics of the DEM in Sec. 2. This includes the creation of overlap free random initial structures [38−40], as well as the two above-mentioned different solution approaches [22]. Next, we introduce, in Sec. 3, the used contact models: A nonlinear Hertzian spring-dashpot (HSD) model [2] and a three parameter Maxwell model, called Maxwell−Zener model (MZ), based on the approach of Radok [28]. In each case, the tangential contact force is based on the theory of MD [31,32]. The HSD model has been used in both the quasi-static and the dynamic solution scheme, while the MZ model has been implemented in dynamic scheme, only.

In Sec. 4, we first consider the contact between two spherical particles by using both contact models to perform quasi-static motion sequences. Furthermore, we investigate the influence of strain rate for the MZ model and compare these results to those of a viscoelastic FEM model [41]. Subsequently, we carry out DEM simulation for a larger particle system consisting of 250 spherical particles.

Based on these studies, the influence of parameters on the dynamic DEM routine is discussed. This includes the choice of material-specific parameters, i.e. density, stiffness and viscosity, and system-specific parameters, i.e. packing factor and coordination number, which have effects on the process-specific parameters, such as time step size and finally on stability, accuracy and duration of the simulation.

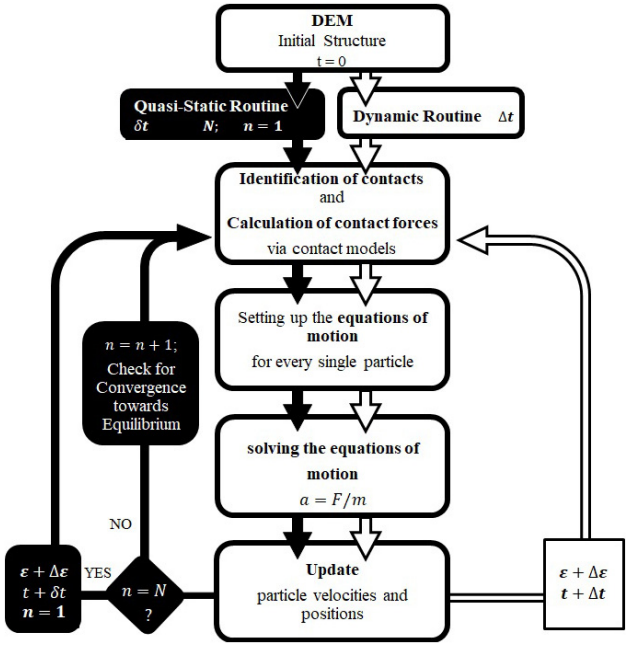

Fig. 1. Flowchart of DEM procedure, separated into quasi-static (left) and dynamic (right) routine. Regarding the quasi-static routine: $N \in \mathbb{N}^+$ represents the fixed maximal number of sub-steps, $n \in \mathbb{N}^+$ is the number of the current substeps.

2. Discrete Element Method

Cundall and Strack [1] introduced in the 1970s the DEM. This numerical procedure uses basic principles of mechanics to describe motion sequences and interactions of discontinuous structures. Newton's equations of motion are solved for all particles individually. Each particle is considered as a discrete element and is uniquely defined by its position in space, translational and rotational velocity, orientation, shape and size. While the computational process takes place at the particle level, the results concerning all single particles can be used to describe the macroscopic behavior of the entire system.

In this numerical scheme, the adopted time step size is limited by the collision time, whilst many macroscopic deformation processes have significantly larger durations, e.g. a quasi-static loading and a creep or relaxation process. Typically to resolve these distinct time scales, different approaches can be adopted as the flowchart in Fig. 1, showing the various steps of the DEM procedure. In the specific case, it refers to a uniaxial compression process of a particle structure simulated by two different approaches, a quasi-static and a dynamic routine. The latter shows the general procedure of the DEM where the process progress is calculated with respect to physical time, while the quasi-static routine represents a sequence of relaxed, i.e. equilibrium states, which has advantages regarding computational stability and accuracy [22,42].

Concerning the general procedure, starting from an initial particle configuration, we assume a strain-controlled scenario for the whole particle assembly by increasing the strain ε by an incremental value $\Delta\varepsilon$ and increasing the physical time t by an incremental value Δt in every step. The granular particles start to move. In our work, we assume all contacts created in this way to be based on the "soft-sphere" approach by Cundall and Strack [1]. The individual particles undergo tiny deformations represented by small virtual overlaps δ_n [27]. In this paper, we consider exclusively overall motion of the

assembly where inertia effects are not relevant, i.e. small strain rates $\dot{\epsilon} = \Delta\varepsilon/\Delta t$.

A contact between two particles with the radii R_i, R_j and a distance d^{ij} exists, if the virtual overlap δ_n has a positive value, i.e. $\delta_n = (R_i + R_j) - d^{ij} \geq 0$, which is numeric reasons actually need to be above a certain threshold. Contacts are determined using appropriate contact point search techniques to speed up the simulation. This is done with neighborhood lists, such as Verlet Lists [43] or Linked Cell methods [44], allowing to exclude in advance contacts of particles which are too far apart from each other. In case of contact, the interaction forces are calculated by choosing suitable contact models. The respective force is decomposed into normal and tangential components and depends geometrical contact properties. The equations of motion are set up for each individual particle and are integrated over time. In general, explicit time integration schemes are used [22]. Acceleration, velocity and position are updated for each particle at each time step Δt. The entire procedure is carried out over a specified time interval. Based on the microscopic results for the contact forces, the macroscopic stress state of the assembly can be calculated as function of macroscopic strain ε.

2.1. Initial packing structure

A configuration of the overall structure before starting the DEM procedure is called initial structure, where the particles occupy the computational domain without interacting with each other. We consider a virtual box filled with a number of particles. Periodic particle arrangement and boundary conditions are assumed in all spatial directions. By means of random packing algorithms such initial structures can be created. Two of them, the random close packing (RCP) algorithm and the drop and roll (DNR) algorithm, are discussed in the following.

The RCP is a two-stage iteration procedure and was first introduced by Jodrey and Tory for spherical particles [38,39]. The initial configuration of this algorithm is defined by a fixed chosen number of particles. Their positions are randomly selected. When starting this algorithm, the value for the packing factor is chosen to be one which, in general leads to a strongly overlapping system. The pair with the largest overlap $\delta_{n,\max}$ is sought in the first step. Besides the current particle radius R_{out}, the inner radius R_{in} is definded as the one which would just give a point contact between the two particles under consideration (see Fig. 2). Based on this, the particles are shifted and reduced in size to eliminate $\delta_{n,\max}$. This process is repeated for the respectively worst overlap in each step until the criterion $R_{\text{out}} \leq R_{\text{in}}$ is satisfied and the algorithm stops. The final packing factor is determined by the so-called contraction rate of size reduction and shifting. The system now corresponds to a densely packed random and overlap free initial structure based on which mechanical DEM simulations can be performed. The RCP has been developed further for assemblies with a size distribution and nonspherical particles in Refs. 45 and 46.

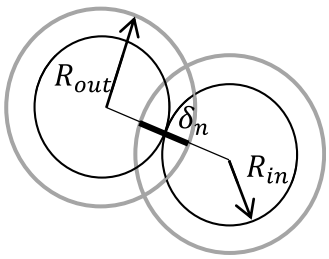

Fig. 2. Illustration of two overlapping particles during RCP procedure with inner and outer radius, R_{in} and R_{out}.

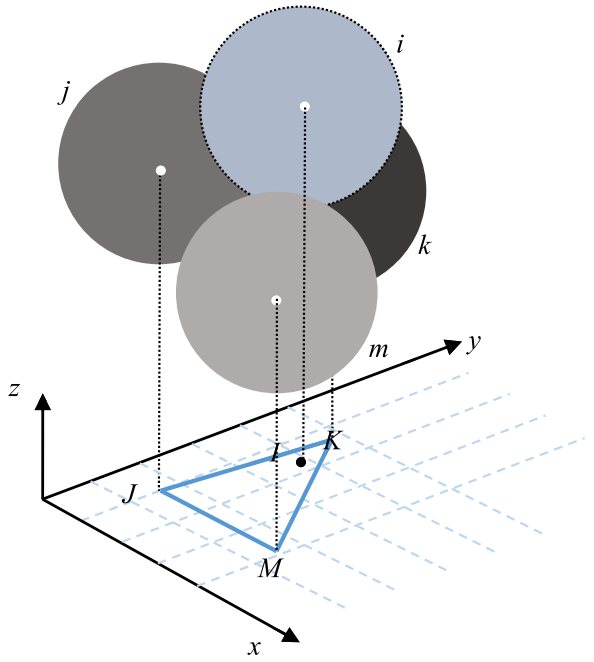

Fig. 3. 3D illustration of DNR procedure: particle *i* drops down searching for a first, second and third contact partner *j, k* and *m*. The stability criterion is reviewed; whether *I* lies within the triangle *JKM* which is defined by the center coordinates produced in a horizontal plane.

The DNR procedure mimics the influence of gravity and is presented as a sequential addition algorithm in Ref. 40. Sequentially, particles are dropped into a predefined virtual box. In our implementation, periodic arrangement of particles enforced in both horizontal spatial directions. The starting position of the dropping process can be uniformly distributed over the top surface of the virtual box. From there, particle *i* falls until it touches the box floor or contacts an already existing particle *j* (see Fig. 3).

If it hits the ground, this is the final position and the next particle falls into the box. If not, particle *i* rolls along the first contact partner *j* in search of a second *k* and, in case of 3D, third contact *m*. If there are three contacts *j, k, m*, there is a possibility of stable position in the existing ball bed. A stability criterion must be checked (see Fig. 3), whether the x, y-center-coordinates of particle *i* lie within the horizontal projected triangle *JKM* produced by its contact partners. Otherwise it will continue to roll until it finds the stable position on the ground or it rolls on until the criterion is fulfilled. If the maximum predefined number of particles is reached, the procedure stops. Subsequently, the box height of the assembly can be varied, so that some particles outside the edges of the volume element are omitted. Geometry and size of the particles as well as the type of distribution of the starting position determine the packing density of the resulting structure.

It should be noted, that in this algorithm periodicity initially exists in both horizontal directions only. To enforce periodicity also in the vertical direction, DEM can be used. The overlaps, which are created due to the demand of periodicity in vertical direction, lead to nonequilibrium contact forces. The particles start to move searching for their energetically most favorable position, which represents the state of equilibrium.

2.2. Solving the mechanical problem

According to Cundall and Strack [1], the dynamic equilibrium is described individually for each particle. For the translational motion, Newton's law is used [47]. The rotational motion of each particle is based on Euler's equations [48]. We do not account for gravity and control the overall, i.e. macroscopic strain of the assembly.

Explicit time integration schemes have proven to be efficient for solving the equations of motion in the numerical DEM problem. An explicit procedure reduces the implementation effort due to its simplicity and robustness. A direct evaluation of nonlinear constitutive laws for the contact forces, a sequential evaluation of all information of each contact pair per time step Δt are among the advantages of such methods compared to implicit ones, as well as avoiding inverting a stiffness matrix. The latter feature means that neither linearization nor a nonlinear equation solver are needed [49].

The leap-frog algorithm is the chosen solution scheme for the translational equations of motion in this work [50]. It is a transformation of the Verlet algorithm and characterized by its low memory requirements as a third order method, which is comparable to the Euler method.

Accelerations $a_{t+\Delta t}$ and positions $x_{t+\Delta t}$ are determined at each full time step $(t+\Delta t)$, whereas the velocities $v_{t+\Delta t/2}$ are calculated offset by half a time step $(t+\Delta t/2)$

$$\boldsymbol{x}_{t+\Delta t} = \boldsymbol{x}_t + \boldsymbol{v}_{t+\Delta t/2}\Delta t, \tag{2.1}$$

$$\boldsymbol{v}_{t+\Delta t/2} = \boldsymbol{v}_{t-\Delta t/2} + \boldsymbol{a}_t \Delta t. \tag{2.2}$$

In order to obtain the velocity at the full time step, the formula can be transformed as

$$\boldsymbol{v}_t = \boldsymbol{v}_{t-\Delta t/2} + \frac{1}{2}\boldsymbol{a}_t \Delta t, \tag{2.3}$$

$$\boldsymbol{v}_{t+\Delta t/2} = \boldsymbol{v}_t + \frac{1}{2}\boldsymbol{a}_t \Delta t. \tag{2.4}$$

In case of rotational motion, the multiplication algorithm is used. This takes into account the change in particle orientation and the associated transformation relationships. At this point, we will not go into detail and refer to further literature [51−53].

2.3. Quasi-static versus dynamic DEM routine

The DEM makes it possible to describe motion sequences of granular structures with respect to physical time t numerically. Figure 1 summarizes the various steps of the DEM simulation procedure, and it is separated into two branches, a quasi-static and a dynamic solution scheme. The entire process is divided into individual load increments depending on the type of external action, whether force-controlled f or strain-controlled ε. In this paper, the latter one is used. The DEM simulation starts at time zero. The system, which is assumed to be a virtual box filled with particles, is still in the resting state (see Fig. 4, middle).

The approach, which describes an infinitely slow motion sequence, is the quasi-static routine (see Fig. 1, left). "Time" used here has no physical meaning, which means time-independent material is especially suitable in this case. The characteristic non-physical time increment is defined as δt. After each incremental strain step $\Delta\varepsilon$, the particles start to move and a static equilibrium state of the structure is sought. All particles are supposed to take an energetically most favorable position. To realize this in the simulation, a subroutine with a predefined number N of substeps is used. In such a substep, a single DEM update is run for all particle positions and velocities. After each single subroutine n, the process is checked for convergence in terms of kinetic energy, contact forces and displacements. After each control, n will be increased by one. The actual process is damped within this subroutine by a non-physical damper until all kinetic energy is removed and to finally reach a static state of equilibrium in the system. When $n = N$, the kinetic energy left in the system is checked. If it is below a certain threshold, the next incremental compression step is initiated. If this is not the case, and there is still kinetic energy inside the system controlled by the convergence criteria, the entire routine terminates.

In order to reach a state of equilibrium in the lowest number of iterations possible, the quasi-static routine starts the iteration by applying each strain increment $\Delta\varepsilon$ by an assumed trial particle configuration (see Fig. 4, left; box compression including a trial configuration (BCT)). BCT produces a complete particle rearrangement: All particles are shifted in the direction of overall strain increment $\Delta\varepsilon$, the magnitude depending on their position in

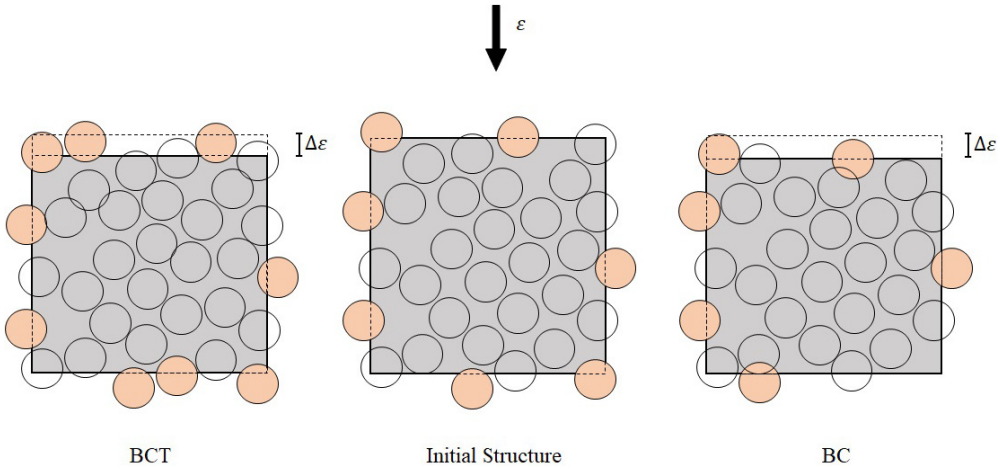

Fig. 4. A two-dimensional illustration of the two different load scenarios BCT (left) and BC (right), which are compared to the initial structure (middle). The latter represents the stress-free starting configuration as created by the RCP or the DNR.

the volume element. This can not only lead to the creation of new periodic particles (orange circles, see Fig. 4), but also to their disappearance or to an exchange of real (not color filled circles, see Fig. 4) and periodic particles. Thus, a smaller number N of steps of the subroutine can be expected which speeds up the DEM procedure for the quasi-static case.

When viscoelastic contact behavior is considered, time t has a physical meaning in the sense that a typical time dependent behavior is associated to viscoelasticity. In this case, the dynamic routine has to be applied where the equations of motion are integrated with respect to physical time t. Concerning the application of strain increment $\Delta\varepsilon$, the BCT procedure as described above can be applied, as well.

A second load scenario represents a more natural compression (see Fig. 4, right; box compression (BC)). Only the upper surface of the particle system is moved according to $\Delta\varepsilon$. As a result, the particles periodically projected from the box bottom to the top move into the box from above thus changing existing contacts or possibly creating new ones while all particles inside the box remain at their position to begin with (Fig. 4, right). In the subsequent DEM step, the position and velocity of all particles are updated by integrating Newton's laws of motion [47] under the action of the contact forces in the physical time interval Δt. Then, without any artificial relaxation process, the next compression step $\Delta\varepsilon$ is applied as before, followed by the next DEM update for time increment Δt.

The main differences between both solution schemes are that after each strain step $\Delta\varepsilon$, BCT and BC result in different particle configuration and that the kinetic energy remains within the system during the dynamic procedure.

2.4. Time step

An uncontrolled and nonphysical increase of energy within a system during a simulated calculation defines an unstable time integration process [49]. The size of the time step Δt has a significant influence on the computational procedure. It should guarantee the stability, accuracy and convergence of such numerical calculations, while all these aspects need to be achieved with a minimum of computational time in order to keep the aspect of costs low.

Concerning the DEM, a critical time step Δt_{crit} has to be defined which may only be chosen that large that each particle is able to influence exclusively its direct neighbors within this time step. This indicates the dependence of Δt on the collision time between two particles. For a normal contact assumption expressed by Hertz [2], assuming two monosized spheres, the Hertzian collision time is defined as [54]

$$t_{\text{Hertz}} = 2.94\left(\frac{5\sqrt{2}\pi\rho(1-\nu^2)}{4E}\right)^{2/5}\frac{r}{v_{0,i}^{1/5}}, \tag{2.5}$$

with the material-dependent values of density ρ, Poisson's ratio ν, Young's modulus E and the respective velocity $v_{0,i}$ before impact. To describe a two-particle contact with sufficient accuracy, the maximum time step Δt_{crit} has to be smaller than 0.5 t_{Hertz} [54].

For an assembly of many densely packed particles, where particles typically have more than one contact, the choice of Δt_{crit} can be expected to depend on the number of contacts. With an increasing number of contacts per particle, called the coordination number, the overall effective stiffness of the system gets larger and the value Δt_{crit} is decreased to ensure an accurately enough simulation [22]. Time steps chosen too large usually lead to strong fluctuations in the solutions, which are no longer meaningful and credible because the exchange of information might not have taken place with the direct neighbors only. This condition must be fulfilled.

According to Belytschko and Hughes [55], the maximum stable time step size Δt_{crit} between two particles is a function of the eigenvalues of the amplification matrix of a linear, undamped single degree of freedom system [49]

$$\Delta t_{\text{crit}} = \frac{2}{\omega_{\max}}. \tag{2.6}$$

Here, $\omega_{\max} = \sqrt{\alpha_{\max}}$ is the maximum value of the frequency and $\alpha_{\max}$ is the maximum eigenvalue of this system. The single degree of freedom system is assumed here to be representative of a single DEM particle. The critical time step is defined as

$$\Delta t_{\text{crit}} = \frac{T}{\pi} = 2\sqrt{m/K_{\text{eff}}}. \tag{2.7}$$

The parameter T denotes the period of an oscillation of this system, m the particle mass and K_{eff} the effective overall stiffness related to the particle motion [49]. Itasca [56] refers in his assumptions to an equivalent single degree of freedom system of point mass and spring, which is infinitely often in series. The formula is

$$\Delta t_{\text{crit}}^{\text{Itasca}} = \beta\sqrt{m/K}. \tag{2.8}$$

In this case, K is the stiffness of the individual contact springs. Itasca extends the theory by multiplying the formula by a safety factor β. This contains problem-specific information. If $\beta = 1.0$, this would not provide a usable time step size for damped methods. Under the conditions of a three-dimensional (3D) damped system that incorporates rotations and translations of the particles, $\beta = 0.17$ shall be chosen. The minimum particle mass and the maximum stiffness with respect to the overall model has to be chosen in Eq. (2.7) [49].

For processes, which show no inertia effects, methods like mass or density scaling can be used to speed up the simulation calculations. By increasing the particle mass or density, the time step size can be increased. This is exclusively suitable for simulations of very slow, i.e. quasi-static processes. The application to high-frequency motion sequences is not suitable for this.

3. Contact Laws

The natural contact behavior, which should be represented as realistically as possible, is influenced by the respective material behavior of the bodies in contact. With the help of rheology, the relationship between stresses and deformations can be described by mathematical models. A mechanical contact pair consists of two particles, which are deformed by their interaction. Regarding the numerical DEM model, this corresponds to two discrete elements connected by rheological models in normal and tangential direction which are assumed to be decoupled [27]. With these models, the forces can be calculated which constitute the components of the resulting contact force.

The basic elements of rheology include the spring, representing elastic behavior, the damper, describing viscous, time-dependent behavior, and the friction element, with which plastic deformations can be transformed into a mathematical expression. By combining these elements, numerous behaviors of fluids and solids can be imitated.

3.1. Elastic contact

In order to describe mechanical contact behavior of two elastic solids in normal direction, the nonlinear theory of Hertz [2] provides an approach. He developed his assumptions in 1880, which still serve as a basis for numerous applications today [5−8]. The contact partners are assumed to have a convex shape and a smooth, frictionless surface, that only a transmission of normal forces can happen. Both bodies are considered as elastic half-spaces [27]. With these predefinitions, the contact can be translated into a mathematical expression. The interaction of the solid bodies occurs exclusively via the contact zone. Furthermore, the assumption of small deformations as well as a small contact area compared to the dimensions of both bodies and principal curvatures of the surfaces in the contact point is valid [27]. Hertz expresses actual deformations in terms of virtual overlaps δ_n [2].

In this work, the shape of all particles corresponds to that of monosized spheres, which is why all the following formulas are given specifically for this particle shape. For spherical particles, the contact area is circular, with the radius a_c. By integrating the pressure distribution $p(x, y)$ over the contact area, the contact force is defined as

$$F_{\text{Hertz}} = \frac{4}{3} E_{\text{eff}} \sqrt{R_{\text{eff}} \delta_n^3}, \tag{3.1}$$

where δ_n is dependent on the contact radius according to $a_c^2 = R_{\text{eff}} \delta_n$. Hertz's solution [2] for the force employs effective material and geometric parameters with respect to both contact partners i and j namely the effective Young's modulus E_{eff} and effective radius R_{eff} defined as

$$E_{\text{eff}} = \left(\frac{1-\nu_i^2}{E_i} + \frac{1-\nu_j^2}{E_j} \right)^{-1} \quad \text{and}$$
$$R_{\text{eff}} = \left(\frac{1}{R_i} + \frac{1}{R_j} \right)^{-1}. \tag{3.2}$$

Translated into a rheological model, Hertz's theory describes the behavior of a nonlinear spring with stiffness $K_n = \frac{4}{3} E_{\text{eff}} \sqrt{R_{\text{eff}} \delta_n}$.

In a quasi-static routine, kinetic energy is dissipated from the system in each subroutine (see Fig. 1, left). This task is performed by a dashpot, which is not assigned any physical meaning. It depends on the size of the virtual overlap δ_n and the coefficient of restitution e which is defined as the ratio of the final to initial relative velocity between a two-particle collision. The rate dependent force for the dashpot is

$$\boldsymbol{F}_{\text{Dashpot}} = -2 \left(\frac{-\ln(e)}{\sqrt{\ln(e)^2 + \pi^2}} \right) \sqrt{\frac{4}{3} E_{\text{eff}} \sqrt{R_{\text{eff}} \delta_n} m_{\text{eff}}} \dot{\boldsymbol{\delta}}_n. \tag{3.3}$$

For the derivation, refer to Ref. 56.

The total contact force in normal direction is then a parallel connection of the nonlinear spring element and nonphysical damper and is here referred to as modified HSD model. In tangential direction, the force−displacement relationship depends on the load history and the instantaneous change in normal and tangential displacement due to the occurrence of tangential slip [31,32]. The tangential force F_t is limited by the magnitude of the friction force F_R, i.e. $F_t \leq F_R$, which follows Coulomb's law, $F_R = \mu F_N$, the product of normal force component F_N and friction coefficient μ. A slip area is formed in the direction of the contact center. If the pressure in the normal direction is high enough, tangential force transmission takes place. If this force component increases, the slip spreads into the adhesion area, up to the state of ideal sliding. Its derivation can be found in Ref. 50. Mindlin and Deresiewicz [31] describe this complex behavior for a numerical iteration procedure over time t with a fixed time step Δt. According to this procedure, the instantaneous shear force is calculated as

$$\boldsymbol{F}_S(t + \Delta t) = \boldsymbol{F}_S(t) + \Delta \boldsymbol{F}_S. \tag{3.4}$$

The change of the shear force $\Delta F_S = 2/3 K_t \Delta \delta_t$ depends on the displacement in tangential direction $\Delta \delta_t = \boldsymbol{v}_t \Delta t$, which depends on the time step Δt itself and furthermore on the relative tangential particle velocity v_t. The minimum of the magnitude of the friction force and the current shear force is chosen as the resulting tangential contact force according to

$$\boldsymbol{F}_t = \min(|\mu \boldsymbol{F}_N|, |\boldsymbol{F}_S(t)|). \tag{3.5}$$

3.2. Linear viscoelastic contact

In theory of materials, viscoelastic material behavior is a combination of elastic and viscous material behavior, which is in general time- or velocity-, load-, frequency- and temperature-dependent [55]. Some characteristic phenomena exist: (i) if stress is kept constant, $\sigma = \sigma' U(t')$, strain $\varepsilon(t)$ will increase with time (creep), (ii) if strain is kept constant, $\varepsilon = \varepsilon' U(t')$, stress $\sigma(t)$ will decrease with time (relaxation). Here, $U(t')$ is defined as unit jump function. This results in the creep compliance $\theta(t) = \varepsilon(t)/\sigma'$ and the relaxation function $\Psi(t) = \sigma(t)/\varepsilon'$. With their help, the material behavior can be described under the influence of abruptly changing input parameters. In case of linear viscoelasticity, the elastic component basically causes spontaneous, limited, reversible deformation, while the viscous component causes time-dependent, unlimited and irreversible deformation [57,58]. Depending on the material, these components are differently pronounced. If the assumption of small deformations is valid, the behavior is similar to linear elastic theory [59]. The Boltzmann superposition principle [60] may be applied, which allows a strain-controlled procedure of a material producing a stress response to be represented as a sequence of individual infinitesimal strain jumps and integrated over time t' [27]. Equivalently, this applies to a stress-controlled process. The material responses can be described by [59]

$$\boldsymbol{\varepsilon}(t) = \int_0^t \theta(t - t') \frac{d\boldsymbol{\sigma}(t')}{dt'} dt', \quad \text{and}$$
$$\boldsymbol{\sigma}(t) = \int_0^t \Psi(t - t') \frac{d\boldsymbol{\varepsilon}(t')}{dt'} dt', \tag{3.6}$$

respectively and are sketched in Fig. 5.

The contact behavior between two viscoelastic solids can be described in an idealized way by combining rheological models. A three-parameter Maxwell model, called MZ model, is suitable for this representation [61]. Figure 6 shows the relaxation function

$$\Psi(t) = E_1 e^{-t/\tau} + E_2 \quad \text{and} \quad \tau = \frac{\eta}{E_1} \tag{3.7}$$

of the MZ model, where τ is the material-specific relaxation time. The relaxation function represents the rate dependence of the model. At the beginning, the relaxation function shows a jump response to a first characteristic value, the spontaneous Young's modulus, which corresponds to the sum of the individual spring stiffnesses, $E_1 + E_2$.

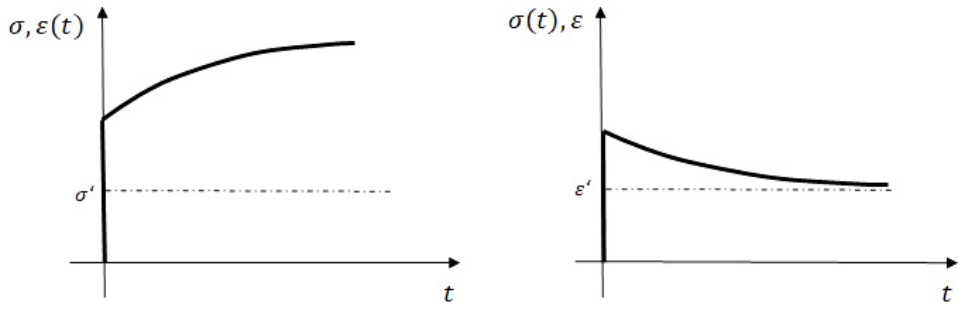

Fig. 5. A schematic illustration of (i) creep and (ii) relaxation.

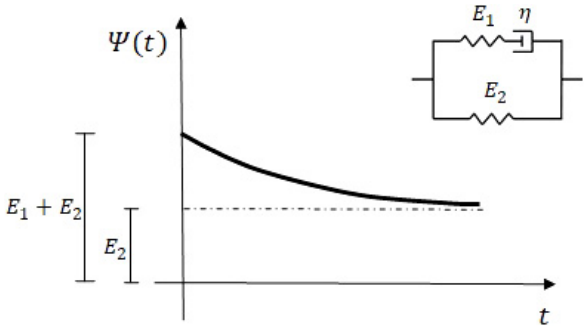

Fig. 6. A schematic illustration of the relaxation function $\Psi(t)$, which defines the behavior of the MZ model due to a constant stress.

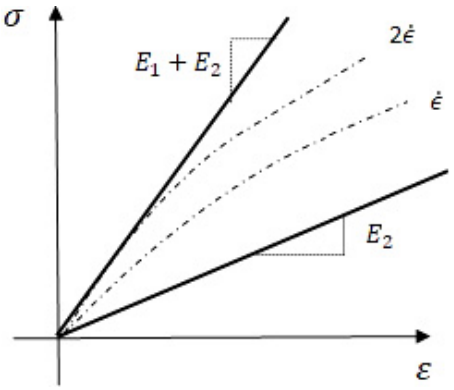

Fig. 7. An illustration of the behavior of linear viscoelastic material behavior under the influence of different strain rates $\dot{\epsilon}$ and the characteristic behavior for a very fast load application, characterized by the spontaneous Young's modulus $E_1 + E_2 = E_{\text{stiff}}$, and for an infinitely slow load application, characterized by the long-term Young's modulus $E_2 = E_{\text{soft}}$.

For $t > 0$, the relaxation function decreases with time and reaches a certain value corresponding to the spring stiffness E_2, the long-term Young's modulus. The dependence on the strain rate $\dot{\epsilon}$ of the stress response as shown in Eq. (3.6) is characteristic for the MZ model. An infinitely slow and an instantaneous increase of strain define the respective stress limit (see Fig. 7). In between, the stress response $\sigma(t)$ for finite strain rates takes place [61]. We call the rheological viscoelasticity model according to Eq. (3.6) the linear MZ model.

In 1957, Radok [28] developed a theory in which he describes mechanical contact on the basis of linear viscoelastic stress−strain behavior. The basic idea is to replace elastic constants in the elastic solution by the corresponding integral operators of the viscoelastic stress−strain relation [61]. The existence of an elastic solution is a prerequisite [27]. In particular, multiplication of two times the shear modulus G_{eff} in the elastic stress response is replaced by a convolution integral employing the time-dependent relaxation function $\Psi(t)$.

The work of Lee and Radok [26] shows such a contact description, in which the Hertz solution [2]

$$F_{\text{Hertz}} = \frac{4}{3} E_{\text{eff}} \sqrt{R_{\text{eff}} \delta_n^3} = \frac{4}{3R_{\text{eff}}} E_{\text{eff}} a_c^3 = \frac{8}{3R_{\text{eff}}} 2G_{\text{eff}} a_c^3 \tag{3.8}$$

was chosen as the elastic solution to be modified to account for the viscoelastic contact behavior with the help of the relaxation function $\Psi(t)$ As mentioned above, replacing $2G_{\text{eff}}$ described as

$$G_{\text{eff}} = 0.5 \frac{E_i E_j}{(1+\nu_i)(2-\nu_i)E_i + (1+\nu_j)(2-\nu_j)E_j}, \tag{3.9}$$

by convolution with the relaxation function $\Psi(t)$ yields

$$F_{\text{Radok}} = \frac{8}{3R_{\text{eff}}} \int_0^t \Psi(t-t') \frac{d}{dt'} a_c(t')^3 dt', \tag{3.10}$$

which fits into the framework of Radok [28].

Inserting the contact radius, $a_c^2(t) = R_{\text{eff}} \delta_n(t)$ and the relaxation function $\Psi(t)$ according to Eq. (3.7) in Eq. (3.10), results in the numerical MZ model as an extension of the elastic HSD model to viscoelasticity. The MZ model used here is based on the assumption of a nonlinear Hertzian spring [2] connected in parallel with a Maxwell model consisting of a nonlinear Hertzian spring and a linear dashpot. The general resulting force from a parallel connection is equal to the sum of the parallel connected models as just described. Based on the elastic solution by using the Hertzian theory [2], the realization is

$$\boldsymbol{F}_{\text{MZ}}(t) = \frac{R_{\text{eff}}}{1-\nu^2} \int_0^t \sum_{i=1}^{2} E_i e^{-\frac{t-t'}{\tau_i}} \sqrt{\delta_n(t')} \dot{\boldsymbol{\delta}}_n(t') dt', \tag{3.11}$$

with i as the numbering of the rheological models connected in parallel, i.e. $i = 1$, indicating the Maxwell model and $i = 2$ denoting the nonlinear Hertzian spring. The prefactor $\frac{R_{\text{eff}}}{1-\nu^2}$ in front of the integral takes into account the Poisson's ratio ν, which assigns the effective material properties to the Young's moduli E_i. It should be noted that this formula refers exclusively to a contact pair of the same material, because ν does not refer to each individual contact particle. Finally, the resulting force for the complete MZ model results from the sum of both models connected in parallel and can

be numerically written as

$$\boldsymbol{F}_{\mathrm{MZ}}(t) = \sum_{i=1}^{2} \boldsymbol{F}_i(t) = \boldsymbol{F}_1(t) + \boldsymbol{F}_2(t), \quad \text{with } \frac{1}{\tau_2} = 0. \tag{3.12}$$

We call the Radok model for viscoelastic normal contact forces according to Eq. (3.11) the nonlinear MZ model. Using the leap-frog algorithm, we obtain for the numerical solution the incremental equations [19]

$$\begin{aligned} i = 1: \quad \boldsymbol{F}_1(t+\Delta t) &= \boldsymbol{F}_1(t) e^{-\Delta t E_1/\eta} + E_1 e^{-\Delta t E_1/(2\eta)} \\ &\quad \sqrt{R_{\mathrm{eff}}\delta_n(t+\Delta t/2)} \\ &\quad \dot{\boldsymbol{\delta}}_n(t+\Delta t/2)\Delta t, \end{aligned} \tag{3.13}$$

$$\begin{aligned} i = 2: \quad \boldsymbol{F}_2(t+\Delta t) &= \boldsymbol{F}_2(t) + E_2\sqrt{R_{\mathrm{eff}}\delta_n(t+\Delta t/2)} \\ &\quad \dot{\boldsymbol{\delta}}_n(t+\Delta t/2)\Delta t. \end{aligned} \tag{3.14}$$

4. Validation of Interparticle Contact Models

To investigate the normal contact behavior, two monosized spherical particles placed exactly on top of each other and are subjected to a uniaxial compression in the direction of their contact by 2% of the box height (see Fig. 8).

In this section, we show that the nonlinear MZ model behaves in an equivalent way to the linear MZ model in the way that the rate dependent response will only occur in a specific range limited by spontaneous and long-term material behavior (see Fig. 7). Figures 9 and 10 illustrate the results in force–displacement and force–time diagrams using different strain rates and also investigation the relaxation behavior. The red curves in both diagrams, Figs. 9 and 10, show the elastic solutions produced via the quasi-static DEM routine using HSD model. The two curves differ in terms of their stiffnesses, $E_s = E_{\mathrm{stiff}}$ and E_{soft}. They represent the spontaneous and the long-term Young's modulus regarding the MZ model (see Fig. 7). The materials used are polyvinylidene fluoride (PVDF) and nickel–manganese–cobalt oxide (NMC). The material data and associated model parameters are listed in Table 1.

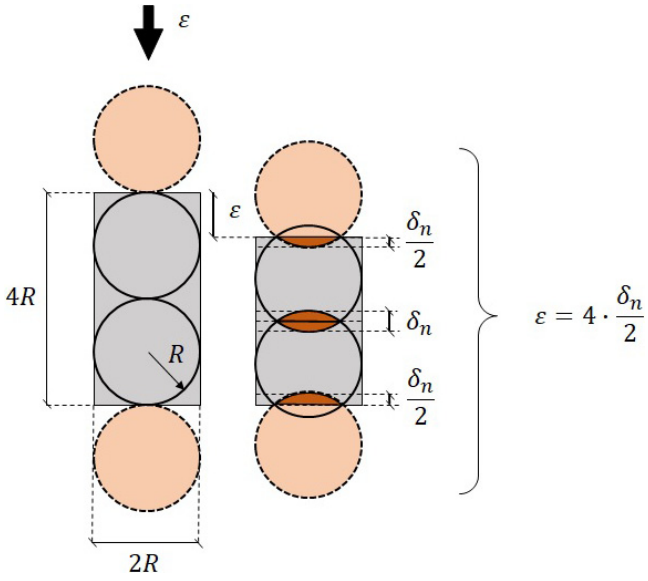

Fig. 8. The relationship of applied strain ε to the virtual overlap δ_n in case of a two-spherical-particle contact visualized in two dimensions. Periodic particles (orange) and real particles (not color filled) in a virtual box of dimensions $2Rx$, $4R$ are shown.

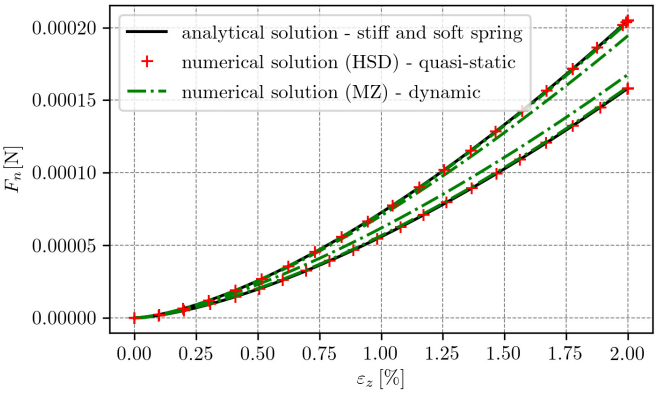

Fig. 9. Comparison of analytical Hertzian solution for the normal contact of two spherical particles to quasi-static HSD solution and to the dynamic solution of the MZ model with variation of the strain rate $\dot{\epsilon}$; HSD (Table 1, PVDF, ρ^{scaled}); MZ (Table 1, PVDF, ρ^{true}); load type: BCT; particle shape: sphere (radius $= 5.0 \cdot 10^{-3}$ mm); compression: 2%; variation of strain rate: $\dot{\epsilon} = [100.0, 10.0, 1.0, 0.1, 0.01]$ 1/s; time step size: $\Delta t = 10 \cdot 10^{-4}$ s.

4.1. Comparison of analytical solution and numerical solution (HSD and MZ)

Figure 9 shows the viscoelastic contact behavior of two PVDF spherical particles. On the horizontal axis the strain of the system is given in % and on the vertical axis the normal contact force is plotted. The reference solutions are assumed to be the solutions calculated by the analytical Hertzian equation (3.1) with Young's modulus chosen as E_{soft} and E_{stiff} according to the values in the caption of Fig. 9, respectively, and they are shown as black solid curves. The overlap δ_n is sequentially increased from 0.0 mm up to the given compression of 2%, which corresponds to an overlap of $\delta_n = 2.0 \cdot 10^{-4}$ mm. This is accompanied by the numerical elastic solutions, red dashed curves, produced via the quasi-static DEM routine while using the HSD model. The analytical and the quasi-static solutions for two different spring stiffnesses E_{stiff} and E_{soft} correspond to the spontaneous and the long-term behavior of the MZ model. The instantaneous stress response of a viscoelastic material occurs due to an abrupt change in applied strain. The long-term solution results from an infinitely slow applied strain. Knowing about the rate dependence of the linear MZ model (compare Fig. 7), we assume that the stress responses for the nonlinear MZ model will behave similarly. This means that the curves resulting under a variation of the strain rate $\dot{\epsilon}$ should also lie between the spontaneous and the long-term stress responses. The exact selected numerical values for the variable input parameter $\dot{\epsilon}$ can be found in the caption of Fig. 9.

To compare the HSD model and the nonlinear MZ model for the long-term behavior, $E_{\mathrm{soft}} = E_2$ must be chosen. To be able to generate the spontaneous stress response with both models, $E_{\mathrm{stiff}} = E_1 + E_2$ must be valid. The task of the linear dashpot regarding the dynamic routine is to dissipate kinetic energy of the system such that a stable converging solution can be produced. In the case that there would be too much kinetic energy inside the system, there is a possibility that the results show oscillations and finally would lose validity.

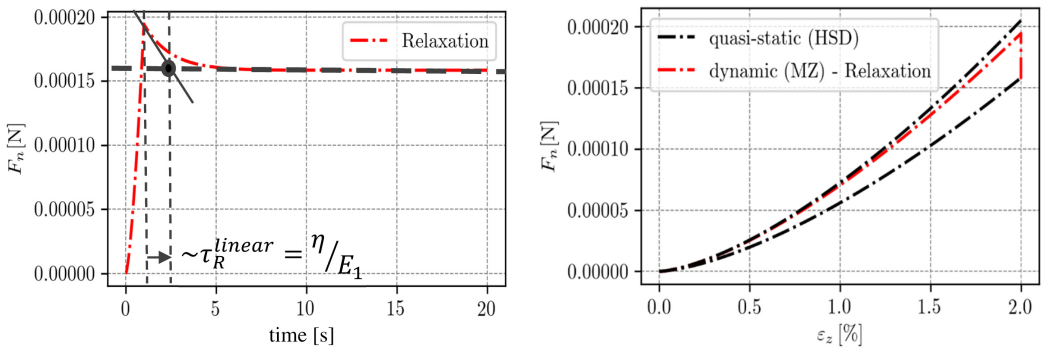

Fig. 10. Relaxation with DEM (dynamic routine, MZ) simulations for contact of two spherical particles (a) including the aspect of relaxation time τ_R^{linear} for linear MZ model and (b) by comparing the behavior with spontaneous and long-term solutions; MZ (Table 1, PVDF, ρ^{true}); load type: BCT; particle shape: sphere (radius $= 5.0 \cdot 10^{-3}$ mm); compression: 2% in 1 s; time step size: $\Delta t = 1.0 \cdot 10^{-4}$ s.

Due to the material selection of PVDF, we assume the same material parameters as in Ref. 62 (see Fig. 9 caption). In this work, the spontaneous and the long-term material behavior was investigated by doing relaxation experiments to identify the parameter values E_1, E_2 and η corresponding to the rheological MZ model. The ratio of η/E_1 defines the relaxation time τ_R and describes the characteristic time needed to approach the steady state or long-term solution [63]. To investigate this behavior, we show a relaxation procedure of the two-particle system according to the nonlinear MZ model. During 1 s, the contact pair is compressed by 2% and the strain is held constant for another 19 s. The normal contact force F_n [N] behavior is plotted against time [s] in Fig. 10(a). It can be assumed that after a duration of three to six relaxation times a completed relaxation should be reached [63], based on the linear MZ model. In this case, τ_R is equal to 1.8 s. This is shown in Fig. 10(a), where the relaxation behavior of the two particle contact is visualized and the corresponding relaxation time τ_R is entered. From a time of about 7.5 s, a constant contact force can be seen, which represents the equilibrium state of the two-particle system. We see that the nonlinear MZ model, which employs two nonlinear Hertzian springs, reflects the same relaxation behavior as the linear MZ model. The same results are visualized in Fig. 10(b) in a force [N] versus strain [%] diagram and are compared to the spontaneous and long-term results produced by dynamic DEM routine while using the MZ model. At a compression 2%, a vertically dropping line is visible in the red graph. This decrease of the contact force shows the relaxation process towards the equilibrium solution.

The green dashed curves in Fig. 9 show the results of the dynamic DEM routine using the nonlinear MZ model and confirm the assumption made earlier that E_{stiff} and E_{soft} also represent the force limits for the nonlinear MZ model. Under variation of the strain rate $\dot{\epsilon}$, the contact force results are exclusively between the limiting solutions, as it is the case for the linear MZ model. The time step size results from formula (2.7) with $\beta = 0.17$ and satisfies the requirement in Sec. 2.4 that $\Delta t_{\text{crit}} < 0.5\ t_{\text{Hertz}}$ during the whole procedure, with $\Delta t_{\text{crit}} = 1.7 \cdot 10^{-4}\,\text{s} < 0.5 \cdot 8.06 \cdot 10^{-2}\,\text{s} = 0.5\ t_{\text{Hertz}}$, and ensures a stable and converging calculation. The load type chosen is BCT, i.e. after each strain step $\Delta\varepsilon$, a particle rearrangement takes place, shifting each particle in the direction of compression depending on its respective position in the assembly as a percentage of the applied strain increment.

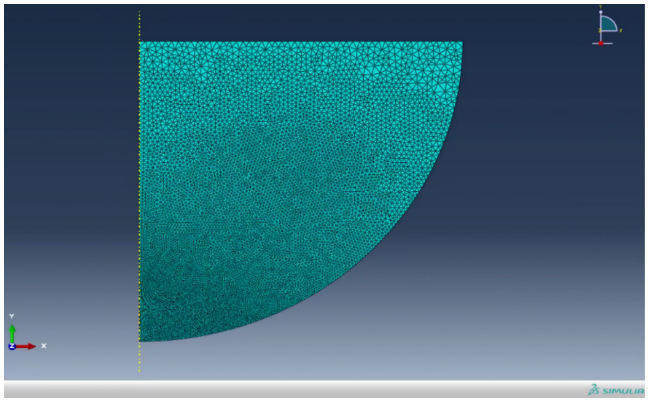

Fig. 11. Discretized FEM model in Abaqus CAE [41].

Table 1. Material properties and model parameters for PVDF and NMC.

	Density [g/mm^3]	Poisson's ratio	HSD (nonlinear spring and nonphysical dashpot)	MZ (nonlinear springs and linear dashpot)
PVDF	$\rho^{\text{true}} = 1.8 \cdot 10^3$ $\rho^{\text{scaled}} = 1.8 \cdot 10^6$	$\nu = 0.4314$	$E_{\text{stiff}} = 1770.5$ MPa $E_{\text{soft}} = 1365.9$ MPa $\eta(\delta_n)$	$E_1 = 404.$ MPa $E_2 = 1365.9$MPa $\eta = 728.28$ MPa s
NMC	$\rho^{\text{true}} = 4.75 \cdot 10^3$ $\rho^{\text{scaled}} = 4.75 \cdot 10^6$	$\nu = 0.25$	$E = 142.0 \cdot 10^3$ MPa $\eta(\delta_n)$	$E_1 = 42.0 \cdot 10^3$ MPa $E_2 = 142.0 \cdot 10^3$ MPa $\eta = 250.0 \cdot 10^3$ MPa s

4.2. Comparison of viscoelastic FEM model to the dynamic solution (MZ)

In Fig. 12, results of the two-particle contact system are produced via an FEM model and a DEM model under the influence of different strain rates $\dot{\epsilon}$. The commercial finite element code Abaqus [41] is used to calculate the numerical solution of FEM by using a Prony series which corresponds to a parallel connection of a spring and a freely selectable number of Maxwell elements. By choosing one Maxwell element only in the Prony series, a comparison to the MZ model used in DEM calculations is possible.

The selected material which is assigned to both particles is PVDF, again. This material shows incompressible material behavior which has the property that under mechanical influence the material changes only its shape while volume remains constant.

Taking advantage of the symmetry of the two particle contact system, see Fig. 8, using an axisymmetric element, a quarter sphere is implemented for the FEM model in Abaqus, see Fig. 11, which has the viscoelastic material properties of PVDF. This is subject to a uniaxial compression of $1.0 \cdot 10^{-4}$ mm on a rigid plane which is a fourth of the complete displacement to yield the overall target strain ε. Regarding the used Prony series to calculate linear viscoelastic constitutive behavior in the FEM solution, we consider one spring with a stiffness E_2 and one Maxwell element is chosen, with the spring stiffness E_1 and the viscosity η. Material-specific Prony parameters g_1 and τ_1 and the spontaneous shear modulus G_0 define the shear relaxation modulus $G_R(t)$, which approximates the time dependent material behavior with a single-term Prony series by

$$G_R(t) = G_0(1 - g_1(1 - e^{-t/\tau_1})), \tag{4.1}$$

where g_1 is the modulus ratio in the first term of the Prony series expansion of the shear relaxation modulus and τ_1 is the relaxation time for the first term of the Prony series expansion. The formulas are [41]

$$g_1 = 1 - \frac{G}{G_0}, \tag{4.2}$$

with the long-term shear modulus G and the spontaneous shear modulus G_0, i.e.

$$G = \frac{3KE_1}{9K - E_1} \quad \text{and} \quad G_0 = \frac{3K - E_1 - E_2}{9K - E_1 - E_2}, \tag{4.3}$$

which depend on the bulk modulus K. The latter value can be derived from the Poisson's ratio ν as

$$K = \frac{-(E_1 + E_2)}{3(2\nu - 1)}. \tag{4.4}$$

The value τ_1 can be calculated as

$$\tau_1 = \frac{9K - E_1 - E_2}{9K - E_1}\tau \tag{4.5}$$

and, among others, it depends on $\tau = \eta/E_1$, the relaxation time, with respect to a Maxwell element, see Eq. (3.7).

In Fig. 12, the black dotted curves represent the contact force behavior while using the nonlinear MZ model in the dynamic DEM routine with two different strain rates to simulate the spontaneous and the long-term behavior again. The model parameters for incompressible PVDF have been taken from [62] which are also used to calculate the relevant parameters $G_0 = 617.5$ MPa, $g_1 = 0.237$ and $\tau_1 = 1.78$ s. As before, the red curves result from the calculation with the HSD model in the dynamic DEM routine using two

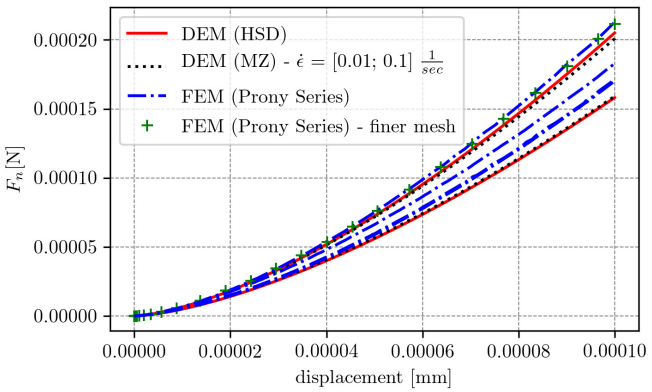

Fig. 12. Comparison of FEM (Abaqus) with DEM (dynamic routine, MZ) simulations for contact of two spherical particles with variation of the strain rate $\dot{\epsilon}$; Prony parameter: $g_1 = 0.237$; $k_1 = g_1$; $\tau_1 = 1.78$ s; HSD (Table 1, PVDF, ρ^{true}); load type: BCT; particle shape: sphere (radius $= 5.0 \cdot 10^{-3}$ mm); compression: $1.0 \cdot 10^{-4}$ mm; variation of strain rate: $\dot{\epsilon}_{\text{FEM}} = [1.0, 0.1, 0.01, 0.001]$ 1/s, $\dot{\epsilon}_{\text{FEM,finer mesh}} = 1.0$ 1/s; time step size: $\Delta t = 1.0 \cdot 10^{-4}$ s.

different stiffnesses, E_{stiff} and E_{soft}. They limit the expected range in which the force responses should run for different strain rates. Varying the strain rate $\dot{\epsilon}$, the results in Fig. 12 show that both models of FEM and DEM (load type BCT, time step size Eq. (2.8)) reflect the typical behavior of the MZ model.

Regarding the reproduction of the limiting curves using FEM, this model presents stiffer solutions. The model is discretized by triangular elements with finer mesh in the direction of the contact point, see Fig. 11. The stiffer behavior of the FEM model suggests that the mesh may need a refinement. By doing this, see Fig. 12, with a low strain rate of $\dot{\epsilon} = 1.0$ (curve of green crosses in Fig. 12), we see an almost identical result to that of the coarse mesh. This means that the coarse mesh already provides a sufficiently accurate solution and a refinement is not necessary which saves valuable calculation time in the case of using FEM. A mesh refinement additionally causes an increasing of the number of nodes which leads to an increasing of the number of degrees of freedom. Due to this, the computational time increases significantly already for the two-particle contact with a computational time of about 3 min, while the DEM has a consistently fast computing time of only a few seconds.

Looking at Fig. 12 again, at the maximum compression of 2%, a percentage difference of about 5.4% between the FEM and the DEM solution for the normal contact of two particles is evident. This stiffer behavior can be explained by the fact that the continuum solution of Abaqus was based on the assumption of incompressible material behavior for PVDF. On the other hand, the formulation of the normal contact force by the nonlinear MZ model according to Radok, does not enforce incompressibility of the deformation a priori.

For an assembly of many particles, an FEM solution with a discretization of each particle by a mesh and the related number of degrees of freedom is computationally expensive in terms of computation time and resources and, thus, generally not feasible. In DEM, on the other hand, each particle is represented by a single degree of freedom. The advantage of the drastic saving of computational cost by this reduction of information on details of the process makes a deviation in the representation of the overall behavior of the assembly by a few percent acceptable. Thus, we come

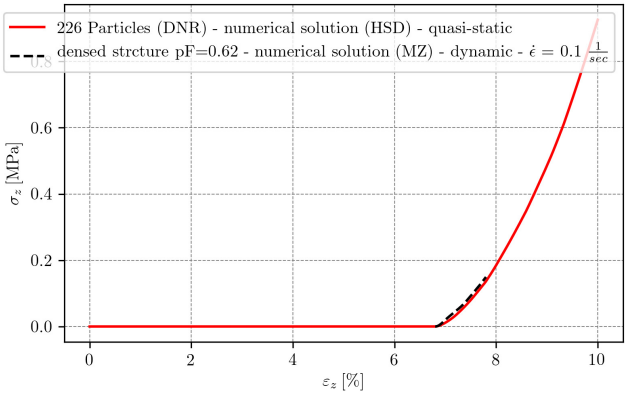

Fig. 13. Configuration produced with DNR. Compression simulation using quasi-static routine and the dynamic routine with HSD model for the normal contact of 226 spherical particles. Packing factor (= pF): [~ 0.58 (red curve) and ~ 0.62 (black dashed curve)]; HSD (Table 1, PVDF, ρ^{scaled}); load type: BCT; particle shape: sphere (radius $= 2.5 \cdot 10^{-3}$ mm); compression: 10% and 1%; time step size: $\Delta t = 1.0 \cdot 10^{-4}$ s.

to the conclusion that DEM provides sufficiently accurate solutions regarding the viscoelastic normal contact using the MZ model.

5. Dynamic Response of Particle Assemblies

In this section, we extend our studies to a larger particle system and also investigate the behavior of this overall structure under the influence of different strain rates $\dot{\epsilon}$. In general, the overall stress response of a large particle structure is also expected to be between two stress limits, the long-term response and the spontaneous response. Furthermore, various influences on the numerical calculation are mentioned, such as the packing density-, the type of load, BCT or BC, and the aspect of the increment size of strain $\Delta\varepsilon$ and time Δt is addressed.

A volume element with 250 monosized spherical particles produced by RCP with a packing density of 0.635 is considered. It can be seen from the literature [64] that this packing density is already close to the upper possible limit of random packings of around 0.64. The particles are therefore no longer able to move freely without coming into contact with other particles. The reason for choosing such a high packing density is to keep the movement space of all particles low in advance in order to largely exclude a growth of the kinetic energy by freely moving particles during the first steps of compression.

The quasi-static routine represents a sequence of equilibrium states, which means that after each load step $\Delta\varepsilon$ any kinetic energy is removed from the system. Looking at structures with low packing density, a rearrangement of the particles first takes place without giving rise to notable interparticle forces. This behavior is shown by the red curve in Fig. 13 below a compression state of 7%. In addition, we use an alternative volume element to demonstrate why we decide to choose high density structures, namely a less densely packed system with 226 particles produced by the DNR, with a packing density of 0.58, is used. During a quasi-static compression simulation of 10%, see Fig. 13, using the HSD model, it is evident that particle rearrangement occurs first while each particle searches for a most favorable position without exerting any mechanical influence on other particles. Looking into Fig. 13, this behavior is related in the diagram to the horizontal stress curve at the constant value zero during a compression from 0% to approx. 7%. Once the structure has been compressed to 7%, where the system now has a packing density of 0.62, the particles experience an elastic strain energy and an initial increase in stress can be seen. This packing density corresponds to a coordination number of about 4.8, which means that each particle should have an average of ~ 5 contact partners to have a sufficiently high packing density and to guarantee a stable simulation result can be produced with our code. As mentioned earlier, we want to study processes where inertia effects due to, say, freely moving particles play no role. To this end, only the configuration reached in this process at 7% represents an initial structure that would allow us to perform comparative calculations between quasi-static and dynamic calculations. This result produced by the dynamic routine is visualized in Fig. 13 with the black dashed curve. It represents a slow compression up to 1% with the compacted structure produced with the quasi-static calculation. The compression state at 7% is taken as the initial structure to simulate the equilibrium solution by using the dynamic routine with the MZ model to confirm the statements made previously. On the other hand, these findings lead us to the conclusion to study densely packed system with 250 particles produced by the RCP, where the initial packing factor is that high that no freely moving particles are present, right from the beginning.

The following diagrams show the respective overall macroscopic stress [MPa]−strain [%] behavior due to a uniaxial mechanical compression of the system by 1% while using the two DEM routines, quasi-static and dynamic, with different contact models, HSD and MZ. The overall stress $\sigma_z = \sigma_{33}$ is calculated from the interaction forces, see Ref. 6. All the following results are based on the use of this volume element. In this paper, we take the well-established quasi-static solution scheme [19,58], while using the HSD model, as a reference for compression simulations on assemblies with elastic contact forces. For quasi-static reference simulations with the HSD model, the density scaling method [22,49] provides the advantage of increasing the inertia of the particles, consequently reducing their velocity and reaching an equilibrium configuration after each load step in less iterations. In our case, while using the HSD model in the quasi-static routine and also in the dynamic routine and the MZ model in the dynamic routine, we scale the density of NMC in every single case from $\rho = 4.75 \cdot 10^3$ g/mm^3, up to $\rho = 4.75 \cdot 10^6$ g/mm^3, while producing quasi-static motion sequences. It is the objective of this section to investigate if the MZ model in the dynamic DEM routine for a large particle system of 250 particles approximates the

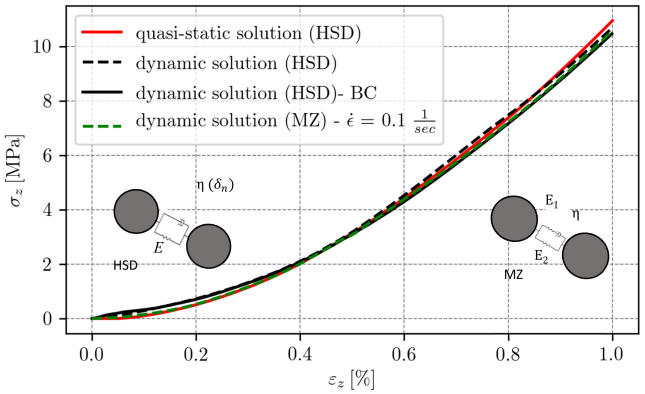

Fig. 14. Comparison of quasi-static solution (HSD) with dynamic solution (HSD) and with dynamic solution (MZ) for contact of 250 spherical particles; HSD (Table 1, NMC, ρ^{scaled}); MZ (Table 2, ρ^{scaled}); load type: BCT and BC; particle shape: sphere (radius $= 2.5 \cdot 10^{-4}$ mm); compression: 1%; packing factor: ~ 0.635; time step size: $\Delta t = 1.0 \cdot 10^{-5}$ s.

associated quasi-static solution using the HSD model with different stiffnesses.

5.1. Quasi-static movement sequences

In order to draw a first comparison of the mentioned implementation variants, the general elastic behavior of NMC particles is investigated first, see also Refs. 19 and 58. The diagram in Fig. 14 represents this elastic stress response of 250 NMC particles. The model and material parameters used are shown in the caption of Fig. 14. Compared are results of the quasi-static routine using the HSD model (red curve) and the dynamic routine, also using the HSD model (black dashed curve). Both rheological models use the stiffness $E = 142.0 \cdot 10^3$ MPa. Additionally, a result of the dynamic routine while using the MZ model (green dashed curve) with $E_1 = 42.0 \cdot 10^3$ MPa, $E_2 = 142.0 \cdot 10^3$ MPa and $\eta = 250 \cdot 10^3$ MPa is represented in the same figure. Here, we use density scaling also in the case of dynamic calculations, since a quasi-static motion sequence is simulated. In the dynamic simulations with the HSD model, a physical loading time of 1 s is chosen, however, this choice should not be of influence, in principle. In the simulation with the MZ model, a long physical time of 10 s is applied to approximate the elastic response for infinitely low loading rates. This choice must be made due to the rate dependency of the MZ model. This choice of simulating a slow procedure confirms the findings on the two-particle contact model that a long loading time, i.e. a low strain rate $\dot{\epsilon}$, tends towards the equilibrium solution of the entire system. The long-term Young's modulus is represented by the model parameter E_2 regarding the MZ model and corresponds to the stiffness E in case of using the HSD model.

The three mentioned simulations are based on the same load type BCT. The black solid curve, on the other hand, shows the result of the dynamic routine using the HSD model, which uses the load type BC. In this case, only the edges of the system are compressed.

In general, all results show a good tendency towards the quasi-static solution using the HSD model which is here defined as reference solution. In detail, it can be seen that the MZ model approximates this reference solution in the initial region better than the curve produced by the HSD model with the dynamic routine. On the other hand, the difference of both curves is less than 5% and this is considered sufficient in this case. Towards the end of the compression, the HSD model calculated with the dynamic routine again approximates the reference solution better. The result of the MZ model reacts minimally softer in this compression area compared to the solution of the HSD model by using the dynamic routine. Using the load scenario BC with the HSD model, the most deviating curve is produced for this case. One possible reason could be the different number of existing contacts, as will be discussed now. As mentioned before, in case of using BCT, all particles are moved in the direction of compression depending on their position in the assembly. Therefore, the probability of contacts occurring is higher compared to the system stressed by BC. On the other hand, the load type, BC, may be understood to reflect a true dynamic process where a system is compressed and is left on its own in a more realistic way. During this procedure, periodic particles appear or disappear and influence the assembly. For large load increments $\Delta\varepsilon$, also depending on the time step size Δt, this can lead to numerical complications as it can no longer be taken as given that each particle affects only its nearest neighbors [2]. Namely, the box compression during a single strain increment $\Delta\varepsilon$ is possibly so large, causing particles center coordinates to be suddenly located outside the volume element boundaries. Our code identifies such events and causes this particle to occur on the opposite side of the volume element due to periodicity. The previously real particle inside the box becomes a periodically projected particle. The new real particle may produce critically large overlaps, which can lead to considerable disturbances in the calculation. The probability of this to happen can be reduced by the BCT load type, because all particles are moved to a trial position at the beginning of the load step. In case of BC, which we understand to induce more something like a wave moving through the assembly, the damping by the chosen rheological model must be high enough to ensure a stable procedure. The load type BCT, on the other hand, with the specification of a trial particle configuration at the beginning of each load step, offers the advantage of representing a system which tends to have similarly large overlaps δ_n everywhere in the assembly with fewer difference in the magnitude of the contact forces occurring, compared to BC. As a consequence and in favor of the BCT load type we find that simulations under this load type have a higher probability of providing a converging solution than using the BC load type. In the latter case, a calculation of the long-term behavior of the structure, i.e. a small time step size for a long process time, which in turn reduces the damping of the system, according to our experience leads to oscillations in the results. The reduction of the damping in the system will be discussed further in the following section while investigating the strain dependent behavior for an assembly of PVDF particles.

As a conclusion of these investigations, it has been confirmed that the MZ model in the dynamic routine is suited to represent quasi-static simulation processes of many particle assemblies. The difference of both load scenarios BCT and BC for the HSD model is about 3% and is acceptable. Due to the above arguments and in view of the minimal difference of the calculation results, the load type BCT will be chosen in the following only.

5.2. Influence of strain rates

The quasi-static motion simulations for NMC illustrated in Fig. 14 were used as a control, since for comparison the behavior of NMC has already been investigated in detail in Ref. 58 and thus serves as a reference point as to whether the MZ model can also reproduce this elastic long-term behavior. While the focus of the results in Fig. 14 was on the load type and the credibility of the quasi-static simulations, here, the focus is on examining the MZ model in terms of strain rate $\dot{\epsilon}$ and time step size Δt. As the MZ model can describe the behavior of viscoelastic materials, we now consider PVDF exclusively. Concerning Fig. 15, the red curves represent the reference solutions produced via the quasi-static routine using the HSD model. Again, two different stiffnesses E_{stiff} and E_{soft} were chosen to represent the spontaneous and the long-term solution with respect to the MZ model regarding the large particle system. The colored dashed curves illustrate the stress responses using the MZ model while varying the strain rate $\dot{\epsilon}$ in a rage of $0.02 - 10.0$ 1/s. After several calculations and investigations of our implemented dynamic DEM routine, it has been found that this range of strain rate reproduces the stress limits of the spontaneous and the equilibrium solution with sufficient accuracy. As justified before, BCT is the only used load type. The parameter values of PVDF [62] can be found in the caption of Fig. 15.

In general, it can be stated that all results produced with the MZ model show a stiffer behavior at the beginning of compression. Basically, this can be explained by the influence of the kinetic energy inside the system simulated by the dynamic procedure. In Fig. 15, a

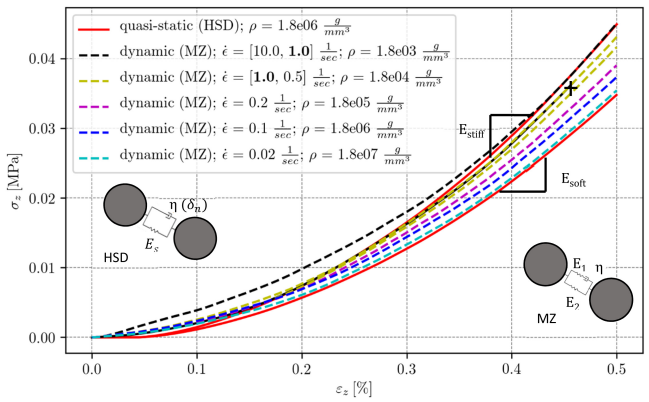

Fig. 15. Comparison of quasi-static solution (HSD) with dynamic solution (MZ) for contact of 250 spherical particles with variation of the strain rate $\dot{\epsilon}$; HSD (Table 1, PVDF, ρ^{scaled}); MZ (Table 1, PVDF, ρ^{true}); load type: BCT; particle shape: sphere (radius $= 2.5 \cdot 10^{-4}$ mm); compression: 0.5%; packing factor: ~ 0.635; variation of strain rate: $\dot{\epsilon} = [10.0, 1.0, 0.5, 0.2, 0.1, 0.02]$ 1/s; time step size: $\Delta t = [1.0 \cdot 10^{-6} - 1.0 \cdot 10 - 4]$ s.

sequence of equilibrium states is compared to a system that is continuously in motion.

While in the quasi-static solution the system is damped after each load step in order to reach the equilibrium state in each sequence, the system of the dynamic routine remains in steady motion, i.e. kinetic energy always exists. In the DEM, it is essential to consider that the time step size Δt should be chosen large enough that each particle can energetically interact with its nearest surrounding neighbors only. Because of this, the time step Δt in the dynamic routine should be chosen much smaller than the nonphysical step size δt in the quasi-static routine. According to the criteria from Sec. 2.4, the time step Δt should necessarily be smaller than half the Hertzian collision time between two particles. If a particle has multiple contact partners in an arbitrarily large system, this can reduce the time step size further, depending on the velocity of the respective particles before the collision. This means that the number of contacts per particle, the coordination number, must necessarily be taken into account when choosing the time step size Δt [22].

A very densely packed system has a large number of contacts already at the beginning of the mechanical compression, which represents a high coordination number, and due to this, there are already high stresses at low compressions. This means that the time step size Δt for a high coordination number must be selected lower than for two contacting particles [49] to be able to describe any information exchange precisely enough.

Another influence are the material specific characteristics, such as the density ρ, the Young's modulus E, and the particle size, i.e. since we are here looking at spheres only, the radius R. Mathematically, these influences can be accounted for using the Itasca definition in Eq. (2.8). The prefactor β originates from investigations in Ref. 49 and takes into account rotation, translation, a 3D system and additionally provides sufficient safety margin. Accordingly, a stiffer material behavior requires a smaller time step Δt. High density and/or large particles increase the time step size. Formula (2.8) is a guide to produce a stable and converging numerical solution, but it does not provide a guarantee. The choice of the time step size is also related to the size of the load increment $\Delta\varepsilon$ to be selected as the strain rate $\dot{\epsilon}$ of the process affects the load increment.

For our simulations, we use density scaling again [22]. The true density of PVDF is $\rho = 1.8 \cdot 10^3$ g/mm^3. Generally, density scaling is used in quasi-static simulations to profit from the higher inertia, which can significantly speed up the computational process. For dynamic calculations, density scaling should be used with caution, as it can distort the results. Namely, the particles do not relax to complete rest between the individual load steps and thus the influence of the high density can falsify the results of the equation of motion. On the other hand, increasing the inertia of the particles could also provide the benefits mentioned, i.e. reducing particle velocities, increasing the time step size and finally accelerate the simulation process. At this point, we will now discuss the numerical background and the influences that advocate density scaling in view of ever slower strain rates up to long-term simulations.

Slow motion sequences are needed to produce the equilibrium solution with the MZ model. By using the true density, these long simulations, according to our experience, exhibit very sensitive numerical behavior and are prone to error. The long process time increases the probability of stress peaks occurring, for example, due to the periodicity that a particle repeatedly moves "in" and "out" of the volume element. Likewise, the kinetic energy can increase abruptly if a particle loses a contact, which means that the rheological model that has existed since then, is also omitted and thus damping no longer takes place, since this rheological model is not active anymore. The values of the model parameters are also an influencing factor. For slow processes employing the MZ model, the term describing the force of the Maxwell model, which includes the damping effect of the linear dashpot, becomes so small that its influence is negligible, see Eq. (3.13). Only Eq. (3.14) is relevant then for such slow motion sequences, which reflects the behavior of the Hertzian spring only, meaning that damping for the control over the stability of the process is largely omitted. When comparing the quasi-static motion sequences between the HSD model and the MZ model, it becomes clear that the nonphysical dashpot of the HSD model which is connected in parallel to the Hertzian spring in the quasi-static routine, provides the numerical stability and ensures convergence of calculations of slow processes. Equation (3.3) shows the complexity and the nonlinear behavior of the used nonphysical dashpot, where the factor of proportionality of $\dot{\delta}_n$ depends on parameters of each individual contact while in the MZ model it is the same material constant for all contacts. It should be mentioned again at this point that the nonphysical damper is only used in the subroutine of the quasi-static routine, where it exclusively pursues the goal of kinetic energy dissipation, such that the quasi-static routine represents a sequence of equilibrium states.

Both formulas, Eq. (3.1) for HSD model and (3.14) for MZ model, describe the behavior of the nonlinear Hertzian spring only. The difference between the two equations is that Eq. (3.1), related to the HSD model, corresponds to a finite equation that depends only on the size of the respective overlap δ_n. For the MZ model regarding Eq. (3.14), Eq. (3.1) is transformed into an incremental equation that now depends on the overlap rate $\dot{\delta}_n$, i.e. the speed of the overlap and the time step size Δt. In addition, Eq. (3.1) and consequently Eq. (3.14) are also not affected by any damping effect. This also explains the sensitive behavior of the dynamic calculations with respect to long-term calculations for the MZ model, whereas in the quasi-static routine the nonphysical damper is active at this point, which is connected in parallel to the nonlinear Hertzian spring seen in Eq. (3.1).

In agreement with the above considerations, it turned out that our calculations with the true density lead to strong oscillations,

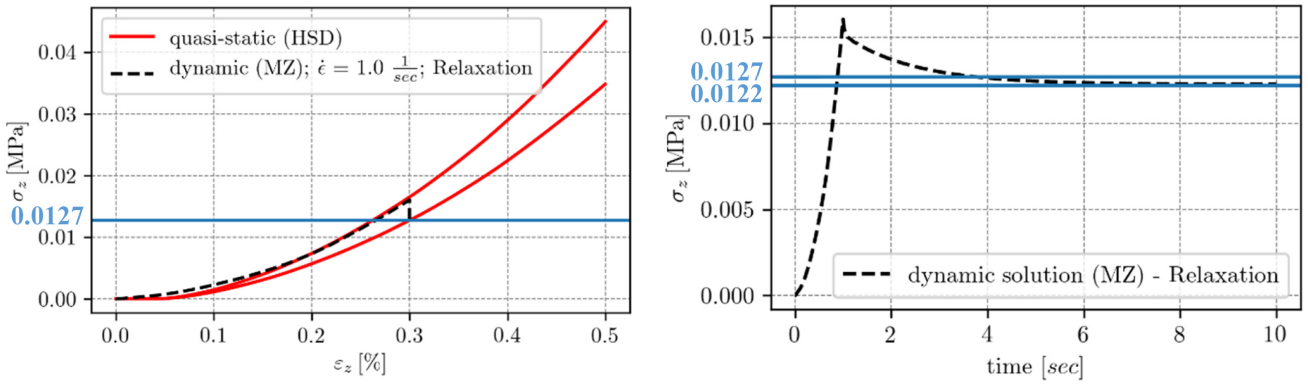

(a) (b)

Fig. 16. Compression of 0.3% in 1.0 s followed by relaxation: dynamic solution (MZ) for contact of 250 spherical particles; HSD (Table 1, PVDF, ρ^{scaled}); MZ (Table 1, $\rho^{\text{scaled}} = 1.8 \cdot 10^4$ g/mm^3); load type: BCT; particle shape: sphere (radius $= 2.5 \cdot 10^{-4}$ mm); packing factor: ~ 0.635; time step size: $\Delta t = 1.0 \cdot 10^{-5}$ s.

especially for small strain rates. The particles are very light and have many movement possibilities due to the long calculation time and the low damping in case of using the MZ model. This advocates the use of density scaling, especially with regard to long-term calculations, since the greater density also allows to increase the time step size and ultimately speeds up the simulation. These results using different densities according to the density scaling method are presented by the colored dashed curves in Fig. 15. The two black curves reflect the results with the true density of PVDF, but two different strain rates where the lower curve belongs to the slower strain rate of 1.0 1/s. Looking at the other dashed curves, the densities are steadily scaled up while decreasing the strain rate, i.e. while ever slower processes approach the long-term behavior of PVDF. This can be seen from the green, violet, dark blue and light blue curves, respectively, where ever greater particle inertia is involved. This growth of density influences the critical time step size, which increases according to Eq. (2.8). Each strain rate has also been calculated with the true density ρ^{true} and the results using density scaling could be validated. However, the simulations using ρ^{true} took longer in each case due to the smaller allowable time step size and, more important, at a certain point of the process exhibited oscillations leading to early termination of the calculation when stress peaks occurred. Only one comparison as described above, is illustrated in Fig. 15, where the black plus "+" at the black dashed curve with $\dot{\epsilon} = 1.0$/s indicates the point of termination. Furthermore, the black and the green curves representing a strain rate of $\dot{\epsilon} = 1.0$/s, demonstrate that an increase of the density by the power of ten yields up to the point of termination using the true density almost the same results (see more details in the legend). This study proves that by density scaling it is possible to present stable and correct results not only for simulating quasi-static processes with the MZ model (see Sec. 5.1), but also for processes with higher strain rates. Due to density scaling the particles get a higher inertial mass. In this way, their velocity is decreased and the possibility of unrealistic oscillations, which produce an unstable numerical calculation, is reduced. Additionally, the time step size is increased and with this the whole simulation time, i.e. wall time, is reduced.

In our calculations, only constant time step sizes were used during an entire simulation. As a further improvement, this could be adapted to the current system conditions, which would mean a reduction of the time increment in the first steps of compression to minimize the kinetic energy and additionally in the higher compression region in Fig. 15, since there are more contacts there.

Finally, we show with these simulation results that the MZ model is also suitable for random particle assemblies and the model characteristic properties of rate dependence can be represented by the MZ model. Due to the increasing simulation time with a growing number of particles, we have limited ourselves to the choice of 250 particles in order to establish meaningful arguments for the choice of the different parameters for such a configuration and to discuss the behavior of this rheological model under the influence of the dynamic routine.

5.3. Relaxation

In Fig. 16, both diagrams illustrate the relaxation behavior of the structure. After a compression up to 0.3% within 1 s, the strain is kept constant for another 9 s. The MZ model is used in the dynamic DEM routine with the load type BCT (black dashed curve, Fig. 16(a)). This result is shown in comparison to the elastic solutions with different stiffnesses calculated using the quasi-static DEM routine and the HSD model (red curves, Fig. 16(a)), where density scaling has been used, as before. Again, the red curves represent the spontaneous and the long-term response of the entire system. In case of using the MZ model in the dynamic DEM routine, the black dashed curve in Fig. 16(a) represents the behavior of 0.3% compression in 1 s of the structure using the strain rate $\dot{\epsilon} = 1.0$/s and a scaled density of $\rho_{\text{MZ}}^{\text{scaled}} = 1.8 \cdot 10^4$ g/mm^3. After a compression up to 0.3%, with the strain being kept constant, the macroscopic response of the assembly shows relaxation. It is to be expected that the value of the stress approaches that of the equilibrium solution, marked with the blue horizontal line, $\sigma_z = 1.27 \cdot 10^{-2}$ MPa, and would remain constant for an infinitely long relaxation (see Figs. 16(a) and 16(b)).

In the stress–strain diagram, the decaying behavior of the structure is evident from the vertical progression of the black dashed curve at constant compression of 0.3%. Thus, the occurrence of the expected relaxation behavior is confirmed, in principle. For more detail, Fig. 16(b) illustrates this behavior again in a stress [MPa]–time [s] diagram. The blue horizontal line illustrates the elastic long-term equilibrium state of the structure. The gray horizontal line shows the value to which the viscoelastic solution seems to converge

in the observed time span. The shape of the black curve confirms the general relaxation behavior, compare Fig. 6. As expected, the viscoelastic solution starts to converge towards the equilibrium solution, but during this process the graph intersects the blue horizontal line, which represents the equilibrium solution of the quasi-static loading process, and approaches asymptotically a value below it. However, the difference between the results shown in Fig. 16(b) is minimal. The first explanation for this deviation is of physical nature. Even though the same assembly is simulated for the quasi-static and the dynamic loading up to 0.3%, the history dependence of the motion patterns in granular systems has to be accounted for. This means that in the same many particle-system the process of quasi-static loading and the process of dynamic loading to the same compression level with subsequent relaxation do not have to lead to the same particle arrangements. Further explanations for the deviation can be of numerical nature like the challenge to calculate long term behavior. A small time step size coupled with a long simulation process, the low damping, here especially by the Maxwell model, see Eq. (3.13), and also the different choice of density can lead to inaccuracies. As a conclusion, we consider the difference of 3% between the two horizontal lines as acceptable inaccuracy in the sense that the MZ model represents the rate-dependent viscoelastic behavior including relaxation even for large particle structures.

6. Conclusion

In this work, a quasi-static and a dynamic DEM routine is explained in detail and implemented numerically in our own code to capture the rate-dependent behavior during compression processes of granular structures. With respect to the mechanical interactions of the individual particles among each other, different normal force contact models are used to describe the respective material behavior, namely time-independent elastic and time-dependent viscoelastic behavior. While time-independent contact force models can be implemented efficiently in the quasi-static routine where no physical time exists, time-dependent contact force models need to be implemented in a dynamic DEM routine in order to preserve the physical meaning of time. In our work, the elastic behavior is modeled by the classical HSD model HSD, while the viscoelastic contact behavior is represented by the nonlinear MZ model. The following conclusions can be made:

(i) As compared to HSD model, the implementation of MZ model in DEM provides rich time-dependent behavior, suitable for many granular structures, where the system responses are sensitive to the loading time, such as calendaring processes for battery cathodes.

(ii) Simulations on a two-particle contact proved that the normal force response of the nonlinear MZ model is also bounded between spontaneous and long-term behavior. The nonlinear MZ model was validated by comparison to finite element simulations of a compressed viscoelastic sphere as exact reference solution of the corresponding continuum mechanics problem.

(iii) The application of the nonlinear MZ model for the normal force behavior in assemblies of many particles brings with it numerical complications that must be taken into account. These include the choice of the load step size as well as the time step size for different strain rates, the loading type and the scaling of density. The critical time step for stable and converging numerical solution is chosen in dependence on the ratio of mass to stiffness, equipped with a stability factor. Thus, while for slow strain rates the general process time increases, the time step remains the same as long as the material and model parameters remain unchanged. In view of this, our investigations showed that for simulation with the nonlinear MZ model with quasi-static strain rates as well as with higher strain rates, density scaling allows for larger time increments to still obtain stable and correct results.

(iv) The time step size Δt in Eq. (2.8) depends only on the material parameters. This quantity Δt remains unchanged for fast and slow loading processes, i.e. quasi-static processes. Due to the linear relationship between load increment and time increment, it becomes clear in case of slow procedures that the time and load increment are relatively smaller compared to fast processes. With regard to the different load types, this argument of the ratio of process time to load or time increment for long-term processes reduces the probability of occurring stress peaks and supports the stability of the numerical calculation.

(v) We have seen that for the numerical simulation of dynamic processes investigated in this work slight changes of influencing factors lead to differences in the results and, thus, they should be chosen with care. These factors are the choice of the packing density of the structure which strongly influences the magnitude of kinetic energy that may occur, the amount of mechanical compression in relation to the packing density, the kind of load type, namely BCT or BC, the choice of strain rate while using the MZ model, as well as density scaling which influences the time step size and can speed up the numerical procedure. Appropriate handling of these factors allows account for viscoelastic contact force behavior via the MZ model in dynamic DEM simulations.

Acknowledgments

This work has been supported by the German Research Foundation (DFG) in the framework of the SiMET research training group (No. GRK 2218/2). This work contributes to the research performed at Center for Electrochemical Energy Storage Ulm-Karlsruhe (CELEST) and was funded by the German Research Foundation (DFG) under project ID 390874152 (POLiS Cluster of Excellence).

References

[1] P. A. Cundall and O. D. L. Strack. Discussion: A discrete numerical model for granular assemblies. *Geotechniquexs* **30**, pp. 331–336, 1980.

[2] H. Hertz. Über die berührung fester elastischer körper (On the contact of elastic solids). *Journal für die reine und angewandte Mathematik* **92**, pp. 156–171, 1881.

[3] D. Antypov and J. A. Elliott. On an analytical solution for the damped Hertzian spring. *Europhysics Letters* **94**, 50004, 2011.

[4] H. A. Navarro and M. P. de Souza Braun. Determination of the normal spring stiffness coefficient in the linear spring–dashpot contact model of discrete element method. *discrete element method. Powder Technology* **246**, pp. 707–722, 2013.

[5] H. Kruggel-Emden, E. Simsek, S. Rickelt, S. Wirtz and V. Scherer. Review and extension of normal force models for the discrete element method. *Powder Technology* **171**(3), pp. 157–173, 2007.

[6] Y. Gan and M. Kamlah, Discrete element modelling of pebble beds: with application to uniaxial compression tests of ceramic breeder pebble beds. *Journal of the Mechanics and Physics of Solids* **58**(2), pp. 129–144, 2010.

[7] D. R. Van Puyvelde. Comparison of discrete elemental modelling to experimental data regarding mixing of solids in the transverse direction of a rotating kiln. *Chemical Engineering Science* **61**(13), pp. 4462–4465, 2006.

[8] R. Y. Yang, R. P. Zou and A. B. Yu. Microdynamic analysis of particle flow in a horizontal in a horizontal rotating drum. *Powder Technology* **130**(1–3), pp. 138–146, 2003.

[9] S. Limtrakul, A. Boonsrirat and T. Vatanatham. DEM modeling and simulation of a catalytic gas–solid fluidized bed reactor: A spouted bed as a case study. *Chemical Engineering Science* **59**(22–23), pp. 5225–5231, 2004.

[10] H. Kruggel-Emden, E. Simsek, S. Wirtz and V. Schwerer. Modeling of granular flow and combined heat transfer in hoppers by discrete element method (DEM). *Journal of Pressure Vessel Technology* **128**(3), pp. 439–444, 2006.

[11] H. Kruggel-Emden, E. Simsek, S. Wirtz and V. Schwerer. A comparative numerical study of particle mixing on different grate designs through the discrete element method. *Journal of Pressure Vessel Technology* **129**(4), pp. 529–600, 2007.

[12] Y. Tsuji, T. Tanaka and T. Ishida. Lagrangian numerical simulation of plug flow of flow of cohesionless particles in a horizontal pipe. *Powder Technology* **71**(3), pp. 239–250, 1992.

[13] R. K. Annabattula, Y. Gan and M. Kamlah. Mechanics of binary and polydisperse spherical pebble assembly. *Fusion Engineering and Design* **87**(5–6), pp. 853–858, 2012.

[14] D. Zhang and W. J. Whiten. An efficient calculation method for particle motion in discrete motion in discrete element simulations. *Powder Technology* **98**(3), pp. 223–230, 1998.

[15] S. Suo, M. Moscardini, V. Becker, Y. Gan and M. Kamlah. Cyclic thermo-mechanical performance of granular beds: Effect of elastoplasticity. *Powder Technology* **394**, pp. 705–713, 2021.

[16] C. Thornton. Coefficient of restitution for collinear collisions of elastic-perfectly plastic spheres. *Journal of Applied Mechanics* **64**, pp. 383–386, 1997.

[17] C. Thornton and N. Zemin. A theoretical model for the stick/bounce behavior of adhesive, elastic-plastic spheres. *Powder Technology* **99**(2), pp. 154–162, 1998.

[18] C. L. Martin. Unloading of powder compacts and their resulting tensile strength. *Acta Materialia* **51**(15), pp. 4589–4602, 2003.

[19] V. Becker and M. Kamlah. A theoretical model for the normal contact force of two elastoplastic ellipsoidal bodies. *Journal of Applied Mechanics* **88**(3), 031006, 2021.

[20] M. Yoshio, R. J. Brodd and A. Kozawa. *Lithium-Ion Batteries*, Vol. 1 (Springer, New York), pp. 2–3, 2009.

[21] S. Hein *et al.*, Influence of conductive additives and binder on the impedance of lithium-ion battery electrodes: Effect of morphology. *Journal of The Electrochemical Society* **167**(1), 013546, 2020.

[22] C. O'Sullivan. *Particulate Discrete Element Modelling: A Geomechanics Perspective* (CRC Press, London), 2011.

[23] O. Birkholz, Y. Gan and M. Kamlah. Modeling the effective conductivity of the solid and the pore phase in granular materials using resistor networks. *Powder Technology* **351**, pp. 54–65, 2019.

[24] T. Kenji *et al.*, Mechanical degradation of graphite/PVDF composite electrodes: A model-experimental study. *Journal of The Electrochemical Society* **163**(3), A385, 2015.

[25] G. Vahabodin *et al.*, Prediction of long-term mechanical properties of PVDF/BaTiO3 nanocomposite. *Journal of Applied Polymer Science* **131**(16), 40596, 2014.

[26] E. H. Lee and J. R. M. Radok. The contact problem for viscoelastic bodies. *Journal of Applied Mechanics* **27**(3), pp. 438–444, 1960.

[27] K. L. Johnson. *Contact Mechanics* (Cambridge University Press, Cambridge, United Kingdom), 1985.

[28] R. J. M. Radok. Visco-elastic stress analysis. *Quarterly of Applied Mathematics* **15**(2), pp. 198–202, 1957.

[29] S. E. Olson. An analytical particle damping model. *Journal of Sound and Vibration* **264**(5), pp. 1155–1166, 2003.

[30] L. Yu, Q. Dai and Z. You. Viscoelastic model for discrete element simulation of asphalt mixtures. *Journal of Engineering Mechanics* **135**(4), pp. 324–333, 2009.

[31] R. Mindlin and H. Deresiewicz. Elastic spheres in contact under varying oblique forces. *Journal of Applied Mechanics* **20**, pp. 327–344, 1953.

[32] A. Di Renzo and F. B. Di Maio. An improved integral non-linear model for the contact of particles in distinct element simulations. *Chemical Engineering Science* **60**(5), pp. 1303–1312, 2005.

[33] K. Goro and K. Kono. Restitution coefficient in a collision between two spheres. *Japanese Journal of Applied Physics* **26**(8R), 1230, 1987.

[34] N. V. Brilliantov *et al.*, Model for collisions in granular gases. *Physical Review E* **53**(5), 5382, 1996.

[35] D. Edward *et al.*, Determination of parameters of a tangential contact force model for viscoelastic spheroids (fruits) using a rheometer device. *Biosystems Engineering* **91**(3), pp. 321–327, 2005.

[36] H. Kruggel-Emden *et al.*, Review and extension of normal force models for the discrete element method. *Powder Technology* **171**(3), pp. 157–173, 2007.

[37] H. Kruggel-Emden, S. Wirtz and V. Scherer. A study on tangential force laws applicable to the discrete element method (DEM) for materials with viscoelastic or plastic behavior. *Chemical Engineering Science* **63**(6), pp. 1523–1541, 2008.

[38] W. Jodrey and E. Tory, Simulation of random packing of spheres. *Simulation* **32** (1), pp. 1–12, 1979.

[39] W. Jodrey and E. Tory, Computer simulation of close random packing of equal spheres. *Physical Review A* **32**(4), pp. 2347–2351, 1985.

[40] J. Zhou, Y. Zhang and J. K. Chen. Numerical simulation of random packing of spherical particles for powder-based additive manufacturing. *Journal of Manufacturing Science and Engineering*, **131**(3), 031004, 2009.

[41] Abaqus. Abaqus user manual (version 6.14). Dassault Systémes Simulia Corp., Providence, RI, 2014.

[42] H. Zhu, Z. Zhou, R. Yang and A. Yu. Discrete particle simulation of particulate systems: Theoretical developments. *Chemical Engineering Science* **62**(13), pp. 3378–3396, 2007.

[43] L. Verlet. Computer experiments on classical fluids. I. Thermodynamical properties of Lennard-Jones molecules, *Physics Review* **159**, pp. 98–103, 1967.

[44] S. Plimpton. Fast parallel algorithms for short-range molecular dynamics. *Journal of Computational Physics* **117**(1), pp. 1–19, 1995.

[45] V. Becker, O. Birkholz, Y. Gan and M. Kamlah. Modeling the influence of particle shape on mechanical compression and effective transport properties in granular lithium-ion battery electrodes. *Energy Technology* **9**, 200086, 2020.

[46] M. Moscardini, Y. Gan, R. Annabattula and M. Kamlah. A discrete element method to simulate the mechanical behavior of ellipsoidal particles for a fusion breeding blanket. *Fusion Engineering and Design* **121**, pp. 22–31, 2017.

[47] J. Berger. *Technische Mechanik für Ingenieure* (Vieweg+Teubner Verlag, Wiesbaden), 1998.

[48] D. Gross, W. Hauger, J. Schröder and W. Wall. *Technische Mechanik 3* (Springer, Berlin), 2012.

[49] C. O'Sullivan and J. D. Bray. Selecting a suitable time step for discrete element simulations that use the central difference time integration scheme. *Engineering Computations* **21**, pp. 278-303, 2004.

[50] J. Matuttis. *Understanding the Discrete Element Method: Simulation of Non-Spherical Particles for Granular and Multi-Body Systems* (John Wiley & Sons), 2014.

[51] F. Zhao and B. van Wachem. A novel Quaternion integration approach for describing the behavior of non-spherical particles. *Acta Mechanica* **224**(12), pp. 3091–3109, 2013.

[52] S. Whitmore and L. Hughes. Closed-form integrator for the quaternion (Euler angle) kinematic equations, US Patent, 2000.

[53] G. Jamshid and R. Barbosa. Three-dimensional discrete element method for granular materials. *International Journal for Numerical and Analytical Methods in Geomechanics* **14**(7), pp. 451–472, 1990.

[54] S. J. Burns, P. T. Piiroinen and K. J. Hanley. Critical time step for DEM simulations of dynamic systems using a Hertzian contact model. *International Journal for Numerical Methods in Engineering* **119**(5), pp. 432–451, 2019.

[55] T. J. R. Hughes and T. Belytschko. A pre´cis of developments in computational methods for transient analysis. *Journal of Applied Mechanics* **50**, pp. 1033–1041, 1983.

[56] Itasca Consulting Group. PFC2D 2.00 Particle Flow Code in Two Dimensions. Itasca Consulting Group, Inc., Minneapolis, Minnesota, 1998.

[57] L. Hale. Principles and techniques for designing precision machines, Ph.D. thesis, University of California, United States, 1999.

[58] V. Becker. Modellierung der mechanik und der effektiven transporteigenschaften von partikulären kathoden sowie deren einfluss auf die elektrochemische performance von lithium-ionen batterien, Ph.D. thesis, Karlsruhe Institute of Technology, Karlsruhe, Germany, 2021. DOI: 10.5445/KSP/1000143718.

[59] H. Parisch. *Festkörper-Kontinuumsmechanik* (Vieweg+Teubner, Verlag, Wiesbaden), 2003. DOI: https://doi.org/10.1007/978-3-322-80052-7.

[60] K. Jan and A. Pegoretti. Proposal of the Boltzmann-like superposition principle for nonlinear tensile creep of thermoplastics. *Polymer Testing* **27**(5), pp. 596–606, 2008.

[61] T. Seelig, Anwendungsorientierte Materialtheorien. Skript zur Vorlesung, 5. Karlsruhe Institute of Technology, Karlsruhe, Germany, 2020.

[62] S. S. Narayan, C. L. Rao and S. M. S. Kumar. Modeling of the viscoelastic properties of PVDF through the fractional differential model. *International Journal of Comadem* **11**(1), pp. 2–8, 2008.

[63] E. Schmutzer. *Grundlagen der Theoretischen Physik. 3. Überarbeitete Auflage* (Wiley-VCH, Weinsheim), pp. 1911–1913, 2005.

[64] Z. Alessio. Explicit analytical solution for random close packing in $\mathrm{d} = 2$ and $\mathrm{d} = 3$. *Physical Review Letters* **128**(2), 028002, 2022.